Ni coarsening in Ni-yttria stabilized zirconia electrodes

Three-dimensional quantitative phase-field simulations supported by ex-situ ptychographic nano-tomography

Yang, Shenglan; Gao, Jianbao; Trini, Martina; De Angelis, Salvatore; Jørgensen, Peter Stanley; Bowen, Jacob R.; Zhang, Lijun; Chen, Ming

Published in:
Acta Materialia

Link to article, DOI:
10.1016/j.actamat.2023.118708

Publication date:
2023

Document Version
Publisher's PDF, also known as Version of record

Acta Materialia 246 (2023) 118708

Contents lists available at ScienceDirect

Acta Materialia

journal homepage: www.elsevier.com/locate/actamat

Ni coarsening in Ni-yttria stabilized zirconia electrodes: Three-dimensional quantitative phase-field simulations supported by *ex-situ* ptychographic nano-tomography

Shenglan Yang [a,b], Jianbao Gao [a], Martina Trini [b], Salvatore De Angelis [b], Peter Stanley Jørgensen [b], Jacob R. Bowen [b,c], Lijun Zhang [a,*], Ming Chen [b,*]

[a] State Key Laboratory of Powder Metallurgy, Central South University, Changsha 410083, China
[b] Department of Energy Conversion and Storage, Technical University of Denmark, Kgs. Lyngby 2800, Denmark
[c] Xnovo Technology ApS, Galoche Alle 15, 1st Floor, Køge 4600, Denmark

ARTICLE INFO

Keywords:
Ni coarsening
Ni-YSZ electrode
Phase-field modeling
Ex-situ ptychographic nano-tomography

ABSTRACT

In-depth understanding of nickel (Ni) coarsening is helpful for improving the service life of Ni-yttria stabilized zirconia (YSZ) electrodes in solid oxide cells. Unfortunately, very few quantitative experimental/theoretical descriptions of Ni coarsening in Ni-YSZ electrodes during long-term operation exist. In this paper, quantitative modeling of Ni coarsening in Ni-YSZ electrodes was achieved through three-dimensional (3D) phase-field simulation supported by *ex-situ* ptychographic nano-tomography and input of reliable thermophysical parameters. A pragmatic procedure was proposed to refine and verify the materials parameters for the simulations. Moreover, the microstructures of the Ni-YSZ electrode in the pristine and annealed states obtained *via* the *ex-situ* ptychographic nano-tomography were used as the initial input and experimental validation for the phase-field simulations. After that, comprehensive comparison between the simulated and the experimental 3D microstructures was conducted, indicating the successful quantitative phase-field simulation of Ni coarsening in Ni-YSZ electrodes presented here. The success of this work is expected to pave the way for accurate prediction of the service life and even design of high-performance Ni-YSZ electrodes.

1. Introduction

Solid oxide cells (SOCs) are electrochemical devices for efficiently converting chemical energy to electrical energy when operated as solid oxide fuel cells (SOFCs), or vice versa when operated as solid oxide electrolysis cells (SOECs). The durability of SOCs during long-term operation is essential for a cost-effective and efficient energy storage [1]. The porous cermet of nickel (Ni) and yttria-stabilized zirconia (YSZ) composite electrode is the current state-of-the-art SOC fuel electrode [2,3]. The composite Ni-YSZ electrode allows the transport of gaseous fuels, ions and electrons simultaneously, facilitating the electrochemical reactions. However, Ni-YSZ electrodes suffer from different degrees of degradation during long-term operation, and their extent of degradation (i.e., degradation rate) depends on the operating conditions, such as temperature, current load, thermal, and chemical and electrochemical gradients. Accordingly, it is still challenging for current Ni-YSZ electrodes to fulfill the actual industrial application requirement of a lifetime of 5–10 years. During the long-term operation at high temperature (600–1000°C), the Ni particles in the active Ni-YSZ electrode coarsen, resulting in both a reduction of the active three-phase-boundary (TPB) density and loss of Ni percolation [4–6]. Thus, the coarsening of Ni particles is considered as one of the most important factors leading to the degradation of Ni-YSZ electrodes. To understand the degradation behavior and even predict the lifetime of the Ni-YSZ electrodes, the quantitative description of the Ni coarsening in Ni-YSZ electrodes during long-term operation is the prerequisite.

Until now, numerous experiments on Ni coarsening in Ni-YSZ electrodes have been conducted aiming at understanding the degradation behavior of Ni-YSZ electrodes [5–18]. Few groups studied the evolution of the Ni particle size as a function of the operating time based on two-dimensional (2D) representations of the three-dimensional (3D) electrode microstructure measured by scanning electron microscopy (SEM) [5–9]. However, important microstructure information is missing in the 2D microstructure. For example, the phase connectivity and/or

* Corresponding authors.
E-mail addresses: lijun.zhang@csu.edu.cn (L. Zhang), minc@dtu.dk (M. Chen).

https://doi.org/10.1016/j.actamat.2023.118708
Received 9 October 2022; Received in revised form 6 January 2023; Accepted 13 January 2023
Available online 15 January 2023

active TPB density cannot be determined from 2D SEM images. Thus, extensive efforts were then devoted to quantifying the Ni coarsening based on the 3D reconstructions of microstructure in electrodes measured by a focused ion beam combined with SEM (FIB-SEM) [10–14] or X-ray tomography [15–17]. De Angelis et al. [18] investigated the Ni coarsening phenomenon of Ni-YSZ electrodes using *ex-situ* ptychographic nano-tomography and obtained the 3D microstructure information at different annealing times during the early stages of annealing. Nevertheless, it is enormously time-consuming and costly to obtain such 3D microstructures experimentally. Furthermore, it is also extremely difficult to acquire the continuous time-dependent 3D microstructure information during the long-time operation of SOCs based on the available experimental techniques. Thus, the quantitative correlation between the degradation behavior and the corresponding microstructure still awaits explication.

In recent years, the phase-field method, as a powerful tool to simulate the microstructure evolution in different materials processes [19–26], has been employed to simulate the Ni coarsening process in Ni-YSZ electrodes [27–32]. In most of the previous studies [27–31], the free energy functional was constructed based on the Ginzburg-Landau equation, and the derivation of the evolution equation follows the conventional Cahn-Hilliard equation for conserved fields. Further, it was assumed in those phase-field models that the YSZ phase is stationary and the Ni-YSZ electrode with three phases can be simplified as the geometry within which only the Ni and pore phases evolve. Therefore, additional boundary conditions for the YSZ interfaces and triple junctions had to be supplemented: (*i*) no-flux boundary at the YSZ interface, and (*ii*) the contact angle boundary condition at the TPB. The smoothed boundary method [33] was usually applied for the solution of partial differential equations in irregular domains with no-flux boundary conditions [27,28,31]. Chen et al. [27], Abdullah et al. [28] and Trini et al. [31] obtained the contact angle boundary condition at the TPB based on Young's condition [34]. Davis et al. [29] and Jiao et al. [30] defined a wetting function accounting for the interaction between the Ni and YSZ phases, which controls the resulting equilibrium contact angle. Lei et al. [32] developed a phase-field model to simulate the microstructure evolution of Ni through the formation and diffusion of gaseous $Ni(OH)_2$ based on the Kim-Kim-Suzuki (KKS) model, but the YSZ phase was treated as rigid walls without further evolution during the simulation and thus an additional boundary condition on the surface of the rigid YSZ phase still needs to be specified to control the contact angle between the Ni and YSZ phases. Furthermore, the above-mentioned phase-field simulations yielded only qualitative or semi-quantitative results. Chen et al. [27] also developed a model considering evolution of the three phases without additional boundary conditions for the YSZ interfaces and triple junctions, but there exists a certain difference between the simulation results and the experimental data. In order to perform a quantitative phase-field simulation of Ni coarsening in Ni-YSZ electrodes, three key factors should be fulfilled [35], i.e., the quantitative phase-field model, input of various reliable thermophysical parameters, and key experimental validation.

Consequently, the major objective of this paper is to perform a quantitative 3D simulation of Ni coarsening in Ni-YSZ electrodes using the multi-phase-field (MPF) model coupled with reliable thermophysical parameters and key experimental validation. Firstly, the MPF model developed by Steinbach and his colleague [20,36,37] is chosen here due to two facts: (*i*) that the MPF model has been widely used in multi-component and multi-phase systems during various materials preparation/service processes [24,38,39], and is quite suitable for simulation of the microstructure evolution in the present three-phase system; and (*ii*) with the MPF model, there is no need to define additional boundary conditions for the phase boundary. Secondly, the microstructures of the Ni-YSZ electrode in the pristine state (i.e. 0 h) and after annealing for 3 h and 8 h at 850°C, obtained previously *via* the *ex-situ* ptychographic nano-tomography by several of the present authors [18], will be used as the initial input structure (i.e., the pristine state) and for validating the phase-field simulations. Thirdly, a pragmatic strategy is proposed to refine and verify various thermophysical parameters required in the governing equations, including bulk energy, diffusion coefficients, interfacial energy, interfacial mobility. The general procedure for the present phase-field simulations is as follows: (*i*) a small 3D sub-volume (i.e., $3.7 \times 3.7 \times 3.7\ \mu m^3$) with an isolated Ni particle taken from the experimentally reconstructed microstructures of the Ni-YSZ electrode is used as the simulation domain to refine the various thermophysical parameters, as the isolated Ni particle presents a convenient system to assess the nature of nickel coarsening and makes the comparison between simulation and experimental results more convenient and straightforward; (*ii*) twelve 3D phase-field simulations on small sub-volumes taken from different locations within the real experimental microstructure of Ni-YSZ electrodes are to be conducted for further verification of the thermophysical parameters; and (*iii*) based on the verified thermophysical parameters, 3D phase-field simulations in the medium and large sub-volumes (i.e., $5.5 \times 5.5 \times 5.5\ \mu m^3$ and $9.2 \times 9.2 \times 5.5\ \mu m^3$) taken from different locations within the real experimental microstructure of Ni-YSZ electrodes are to be performed. The cumulative particle size distributions (PSDs) and TPB tortuosity evolution for all phases in the medium and large sub-volumes of the experimental microstructure are analyzed and utilized to validate the phase-field simulations.

2. Experimental

The sample was prepared from a Ni-YSZ anode supported SOFC half-cell. The starting NiO-YSZ cermet was reduced for 1 h at 850 °C in a mixture of 9% H_2 in N_2. Details of the cell production can be found in Ref. [40]. The functional layer of the cell is ~15 μm with a nominal reduced composition of Ni/8YSZ, where 8YSZ corresponds to 8 mol.% Y_2O_3 doped zirconia. A cylindrical pillar sample with a diameter of ~14 μm and a height of ~15 μm was produced via FIB milling to create a representative volume of interest. The sample was secured on a modified standard cSAXS beam line sample holder. Details of the sample preparation and characterization can be found in Ref. [18]. The ptychographic X-ray computed tomography experiment was performed using the X12SA (cSAXS) beamline at the Swiss Light Source, Paul Scherrer Institute, Switzerland. For further details on the instrumentation, one can refer to Ref. [41]. The sample was imaged in the pristine state and after annealing of 3 h and 8 h at 850 °C in a gas mixture of 4% H_2 and 96% N_2. The heat treatments were conducted in a small custom-made tube furnace with a flow rate of 5 1/h and the heating and cooling rate was controlled to 10 °C/min. The experimentally reconstructed 3D microstructures of the Ni-YSZ electrode in the pristine state and after annealing for 3 h and 8 h have the volume of $9.2 \times 9.2 \times 9.2\ \mu m^3$ (see Fig. S1 in the supplementary materials).

3. Model description

3.1. Multi-phase-field model

The Ni-YSZ electrode is composed of three phases, i.e., a pore phase, an oxygen ion conducting phase (i.e., YSZ), and an electron conducting phase (i.e., Ni). In the present phase-field simulation, the pore phase is treated as a gas phase, while Ni and YSZ phases are solid phases. With regard to the energy term, only chemical energy and interface energy are considered in this system. The total free energy functional consists of interfacial energy f^{intf} and chemical energy f^{chem} [20,36,37], and can be formulated as the following:

$$F = \int_{\Omega} f^{intf} + f^{chem} \tag{1}$$

$$f^{\text{intf}} = \sum_{\alpha,\beta=\text{pore,YSZ,Ni},\alpha\neq\beta} \frac{4\sigma_{\alpha\beta}}{\eta_{\alpha\beta}} \left\{ -\frac{\eta_{\alpha\beta}^2}{\pi^2}\nabla\phi_\alpha\cdot\nabla\phi_\beta + \phi_\alpha\phi_\beta \right\} \quad (2)$$

$$f^{\text{chem}} = \sum_{\alpha=\text{pore,YSZ,Ni}} h(\phi_\alpha) f_\alpha(c_\alpha) + \tilde{\mu}\left(c - \sum_{\alpha=\text{pore,YSZ,Ni}} \phi_\alpha c_\alpha \right) \quad (3)$$

where ϕ_α is the phase field value of α phase/grain and the sum constraint $\sum_{\alpha=\text{pore, YSZ,Ni}} \phi_\alpha = 1$ is always satisfied. $\sigma_{\alpha\beta}$ is the interfacial energy between α and β phases/grains, while $\eta_{\alpha\beta}$ is the interfacial width and is treated to be equal for all interfaces. $h(\phi_\alpha)$ is a monotonous coupling function. $f_\alpha(c_\alpha)$ is the bulk free energy density of the individual phase, depending on the phase concentrations c_α of solute Ni, and can be obtained from either the thermodynamic database or the linear phase diagram. $\tilde{\mu}$ is the diffusion potential of component Ni introduced as a Lagrange multiplier to conserve the mass balance between the phases $c = \sum_{\alpha=\text{pore,YSZ,Ni}} \phi_\alpha c_\alpha$.

Based on the free energy functional shown in Eqs. (1-3), the MPF governing equations can be derived as [20,36,37],

$$\dot{\phi}_\alpha = \sum_{\beta=\text{pore,YSZ,Ni}} \mu_{\alpha\beta} \left\{ \sigma_{\alpha\beta} \left[\phi_\beta\nabla^2\phi_\alpha - \phi_\alpha\nabla^2\phi_\beta + \frac{\pi^2}{2\eta^2}(\phi_\alpha - \phi_\beta) \right] + \frac{\pi}{\eta}\sqrt{\phi_\alpha\phi_\beta}\Delta g_{\alpha\beta} \right\} \quad (4)$$

$$\dot{c} = \nabla \sum_{\alpha=\text{pore,YSZ,Ni}} \phi_\alpha D_\alpha \nabla c_\alpha \quad (5)$$

where $\mu_{\alpha\beta}$ is the interface mobility between α and β phases. $\Delta g_{\alpha\beta}$ is the local deviation from thermodynamic equilibrium and given as,

$$\Delta g_{\alpha\beta} = -f_\alpha(c_\alpha) + f_\beta(c_\beta) + \tilde{\mu}(c_\alpha - c_\beta) \quad (6)$$

D_α is the chemical diffusion coefficient of α phase. In fact, Eq. (4) cannot be directly derived from the free energy functional, but is a so-called antisymmetric approximation, which resigns from thermodynamic consistency at the multiple junctions [20]. This is commonly done in most MPF simulations [20].

3.2. Numerical settings and materials parameters

All the phase-field simulations in the present work were carried out in a 3D domain with different sizes. The experimentally reconstructed microstructure of the Ni-YSZ electrode at 0 h was used as the initial simulation microstructure. Since the entire experimentally reconstructed 3D microstructure of the Ni-YSZ electrode (see Fig. S1 in the supplementary materials) has a large number of grid points (501 × 501 × 501) with a very small pixel size of 0.0184 μm, it would be very time-consuming if the experimentally reconstructed grid spacing is directly adopted for phase-field simulations. In order to accelerate the numerical simulation, the grid spacing was rescaled to 0.037 μm in the phase-field modeling. The interface thickness is set to 0.148 μm. Moreover, the periodic boundary condition was applied to the boundaries of phase and composition fields in each direction.

Currently, there is no phase diagram of the Ni-YSZ-Gas system available in the literature, not to mention the corresponding thermodynamic descriptions. Therefore, a hypothetical linear phase diagram was assumed for the present phase-field simulations. In fact, the YSZ is an inert phase in the Ni-YSZ electrode, and thus the phase diagrams for describing the Ni/YSZ and YSZ/gas interactions can be arbitrary for Ni coarsening in the Ni-YSZ electrode. Hence, only a linear phase diagram was assumed for the Ni/gas interaction (see Fig. S2 in the supplementary materials). The simulation composition was determined by the lever rule based on the phase fractions of Ni and pore (gas) in the Ni-YSZ system, while the simulation temperature is in accordance with the experimental one (i.e., 850°C). The diffusion coefficient of Ni in the pore phase, interfacial energy and interface mobility were optimized in the phase-field simulation of the isolated Ni particle through minimizing errors between phase-field simulated and experimental results. The diffusion coefficient of Ni in pore phase were optimized in magnitude between the Ni bulk diffusivity (~10^{-16} m^2 s^{-1}) and the Ni surface diffusivity (~ 1.4 × 10^{-11} m^2 s^{-1}) [42].

3.3. Strategies for validating simulated microstructures

The key experimental validation of simulated microstructures is one of the prerequisites of quantitative phase-field simulations. In order to validate the reliability of the phase-field simulated microstructures, two strategies were utilized in the present study for comparison between the simulation and experimental results.

The microstructure information of phase-field simulated microstructures was compared with experimental data, which is the general method for comparison between simulation and experimental results. In the simulation of the small sub-volumes with the isolated Ni particle, the comparisons between typical microstructure features (i.e., volume, surface area, and average radius etc.) of the isolated Ni particle in phase-field simulated and experimental small sub-volumes were performed. Various microstructure parameters including phase fraction, interface areas of single/dual phases, and TPB density are characteristic parameters for describing a porous complex multiphase microstructure. Hence, various microstructure parameters of small, medium and large sub-volumes on the phase-field simulations were compared with experimental data. The PSD for the Ni phase can statistically display the Ni coarsening. Moreover, the connectivity of phases and phase boundaries in Ni-YSZ electrodes play an essential role in their gas, ion and electron transport, and thus electrochemical reaction efficiency, and TPB tortuosity can representatively demonstrate the connectivity of TPB in microstructures. Therefore, the cumulative PSDs and TPB tortuosity for all phases in medium and large microstructures from the phase-field simulations were compared with experimental data. The definition and calculation methods of various microstructural parameters, the cumulative PSD, and TPB tortuosity are described in Refs. [18,43].

In this work, a new strategy for a quantitative comparison between the simulated microstructures and the experimental ones was proposed. The phase field variable $\phi(t, \vec{x})$ was utilized as a variable of the comparison. In the simulated and experimental microstructure, the phase field variables of the pore, YSZ and Ni phases are defined as three different values, respectively. A relationship for quantifying the difference between the simulated and experimental microstructures is proposed as,

$$\phi_{\text{sim}}(t, \vec{x})\cdot N_{\text{pha}} + \phi_{\text{exp}}(t, \vec{x}) = \delta_{\text{dis}}(t, \vec{x}) \quad (7)$$

where $\phi_{\text{sim}}(t, \vec{x})$ and $\phi_{\text{exp}}(t, \vec{x})$ are the phase fields of the simulated and experimental microstructures, respectively, N_{pha} is the number of phases in the system, and $\delta_{\text{dis}}(t, \vec{x})$ is the parameter to distinguish the simulated and experimental microstructures. The experimentally reconstructed microstructure has the sharp interface, while the simulated microstructure has the diffusive interface. In other words, when across the interface, the field variable has the abrupt change in experimentally reconstructed microstructures, but the continuous change in simulated ones. In order to make the comparison straightforward, $\phi_{\text{sim}}(t, \vec{x})$ over the interface region of the simulated microstructure needs to be approximated. The phase field variable $\phi_{\text{sim}}(t, \vec{x})$ for the pore, YSZ and Ni phases in simulated microstructures were denoted by 0, 1 and 2, respectively, and $\phi_{\text{sim}}(t, \vec{x})$ with the highest fraction was given in the interface region. $\delta_{\text{dis}}(t, \vec{x})$ in Eq. (7) was given as a combination of the unique number between 0 and 8 for the microstructure of Ni-YSZ electrodes. When the simulated pore, YSZ or Ni evolution is consistent with the experimental result, i.e. the simulated phase field, $\phi_{\text{sim}}(t, \vec{x})$, is equal to $\phi_{\text{exp}}(t, \vec{x})$, to be 0, 1 or 2, then the $\delta_{\text{dis}}(t, \vec{x})$ is equal to 0, 4 or 8, respectively. The values of $\delta_{\text{dis}}(t, \vec{x})$, $\phi_{\text{exp}}(t, \vec{x})$ and $\phi_{\text{sim}}(t, \vec{x})$ for the

comparison were listed in Table S2 in Supplementary materials.

4. Results and discussion

4.1. Benchmark test of materials parameters

A microstructure with a small 3D domain of $3.7 \times 3.7 \times 3.7$ μm^3 containing an isolated Ni particle (see Fig. 1a and b) taken from the real microstructure of Ni-YSZ electrodes at 0 h was utilized as the initial input to phase-field simulation, and those at 3 and 8 h for subsequent comparison of microstructure evolution. A large number of phase-field simulations of the isolated Ni particle were implemented based on the inputs of numerous sets of thermophysical parameters including interfacial energies available in the literature [44–47]. The morphology and typical microstructure features of the isolated Ni particle on each phase-field simulation were compared with the experimental result. Then, a set of thermophysical parameters was selected from the numerous ones used for the simulations, which obtained the minimum relative error between the simulated and experimental microstructural features of the isolated Ni particle. All selected thermophysical parameters were further optimized through minimizing the relative error between phase-field simulated and experimental microstructure features of the isolated Ni particle. The refined thermophysical parameters are listed in Table S1 in Supplementary materials, and the evolution of the phase-field simulated isolated Ni particle based on them were shown in detail in Figs. 2 and S3 (in Supplementary materials) below.

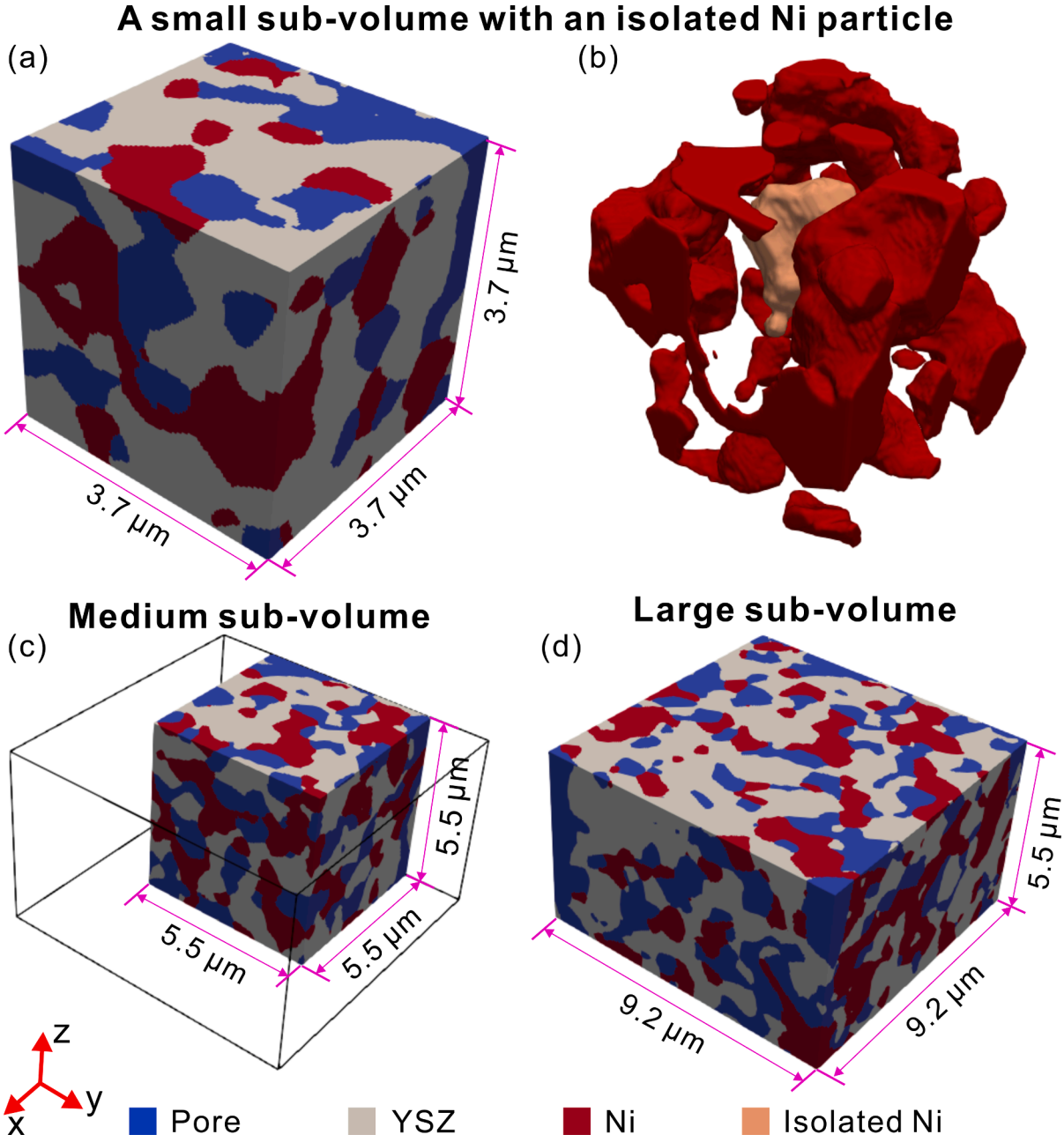

Fig. 1. Representative 3D microstructures taken from a real microstructure of the Ni-YSZ electrode. (a) a small sub-volume with a domain of $3.7 \times 3.7 \times 3.7$ **μm**^{3} containing an isolated Ni particle; (b) the same volume as in (a) showing only the Ni phase and the isolated Ni particle (i.e. the pore and YSZ phases are transparent); (c) a medium sub-volume with a domain of $5.5 \times 5.5 \times 5.5$ **μm**^{3}, and (d) a large sub-volume with a domain of $9.2 \times 9.2 \times 5.5$ **μm**^{3}. The blue region is the pore phase, the gray region is YSZ phase, the red region is Ni phase, and the orange region is the isolated Ni particle. (For interpretation of the references to colour in this figure legend, the reader is referred to the web version of this article.).

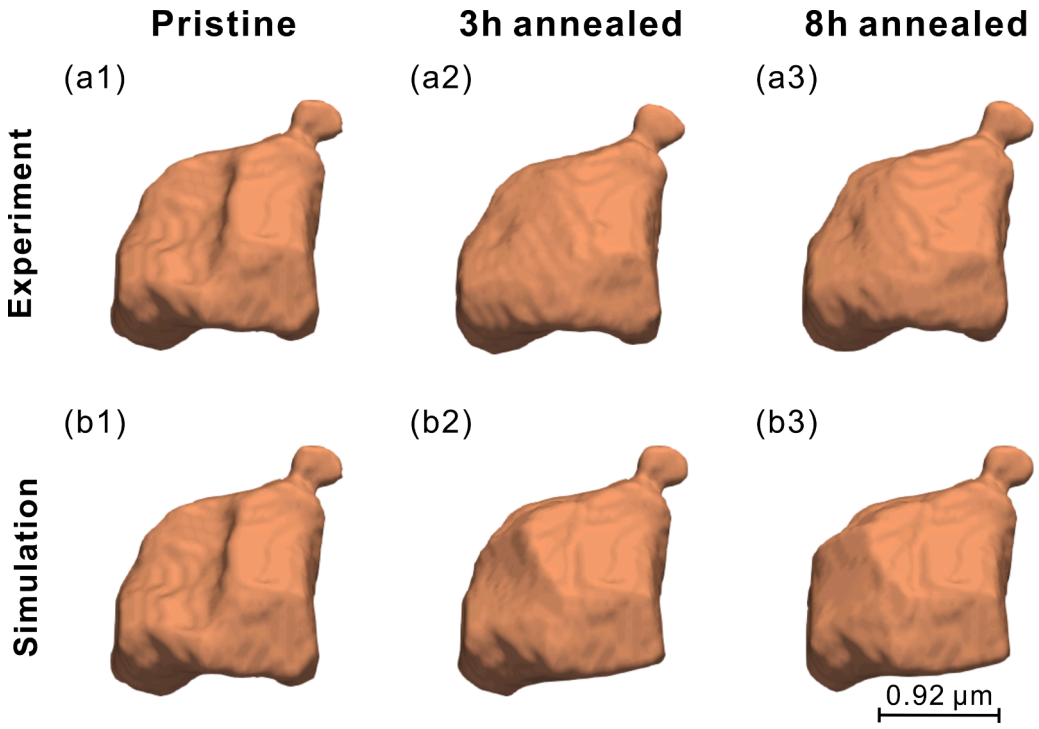

Fig. 2. 3D Morphology evolution of the isolated Ni particle in the microstructure shown in Fig. 1a and b. Experimental: (a1) Pristine state, (a2) after annealing at 850 °C for 3 h, and (a3) for 8 h; Phase-field simulation: (b1) Pristine state, (b2) after annealing for 3 h, and (b3) for 8 h.

Fig. 2 displays the morphology evolution of the isolated Ni particle in the phase-field simulated small sub-volume, compared with the corresponding experimental morphologies. As shown in Fig. 2 (a1) and (b1), the simulated isolated Ni particle in the pristine state is identical to the experimental one. As the aging time increases, the curvature of the isolated Ni particle decreases, but does not change significantly between 3 and 8 h. The concave surface of the isolated Ni is gradually filled and becomes convex. It can be seen in Fig. 2 that the curvatures of the simulated isolated Ni particle at different annealing times fit with experimental results. The volume, surface area and average radius of the isolated Ni particle in the phase-field simulated small sub-volume were calculated and compared with results of the isolated Ni particle in the real experimental microstructure (see Fig. S3 in Supplementary materials). For the period of 0–3 h annealing time, the volume and average radius of the isolated Ni particle on the phase-field simulation increase, whereas the surface area decreases first, and then increases after about 0.4 h. That is because the local microstructures of the isolated Ni particle in the pristine state have the larger curvature, which decreased rapidly when the simulation started. The decrease of curvature introduces decrease of surface area. The observed increase in Ni surface area is attributed to the Ni/YSZ interface. When the Ni closes small pore cavities and forms Ni/YSZ interfaces, it is forced to follow the surface morphology of the YSZ. Both the faceted surface of the YSZ and its increased roughness originating from a segmentation result in an increased interface area compared to a Ni/pore interface where the Ni is free to minimize its surface unconstrained. Such two effects are in competition with each other. From 3 h onwards, the volume, surface area and average radius of the isolated Ni particle slightly change, and the phase-field simulation results agree well with the corresponding experimental data at different annealing times. The maximum relative errors between simulated and experimental results for the volume, surface area and average radius of the isolated Ni particle at different annealing times are below 6%, 2%, and 2%, respectively (see Fig. S3 in Supplementary materials). It should be emphasized that calibrating/validating a model with an isolated Ni particle is very valuable as it reduces the number of free parameters and thus gives strong confidence to the model when it agrees with experimental data.

Twelve small microstructures with a 3D domain of $3.7 \times 3.7 \times 3.7\ \mu m^3$ (like the sub-volume shown in Fig. S4 in Supplementary materials) taken from different locations within the real experimental microstructure of the Ni-YSZ electrode in the pristine state were used as initial input of simulations aiming at confirming the reliability of the thermophysical parameters. The microstructure parameters of these phase-field simulated sub-volumes were calculated, and their maximum and minimum values were used as the upper and lower limits of the uncertainty due to the structural heterogeneity from different locations in the real Ni-YSZ electrode microstructure, as shown in Fig. 3. Similarly, the microstructure parameters of a large number of small sub-volumes taken from different locations within the real experimental microstructure in the pristine state and after 3 and 8 h of annealing were calculated and superimposed on Fig. 3, and their maximum and minimum values were used as the upper and lower limits of the uncertainty. From Fig. 3a–c, it is evident that the phase fractions of Ni, pore and YSZ phases from the phase-field simulated microstructures remain unchanged as the annealing time increases, which satisfies mass conservation. From Fig. 3d–f, it can be seen that interface areas of the pore and Ni phases per unit volume gradually decrease as the annealing time increases, while that of YSZ phase does not change. From Fig. 3g–i, it is seen that the pore/YSZ interface area per unit volume increases as the annealing time increases, while the pore/Ni and Ni/YSZ interface areas per unit volume decrease. From Fig. 3j and k, it is apparent that the total TPB density decreases as the annealing time increases, while the percolating TPB density first increases before about 0.5 h of annealing and then decreases. The reason might be that the Ni coarsening (i.e., loss of the connectivity of the Ni network) resulted in the improvement of the connectivity of the pore network and thus previously isolated TPBs become percolated [18]. This effect is counter balanced by the reduction of the total TPB density. A considerable reduction of total TPB density can lead to the reduction of the percolating TPB density as the annealing time increases. As shown in Fig. 3, the trends of the microstructure parameters of the phase-field simulated microstructures with annealing time agree with those of more than 200 small sub-volumes taken from

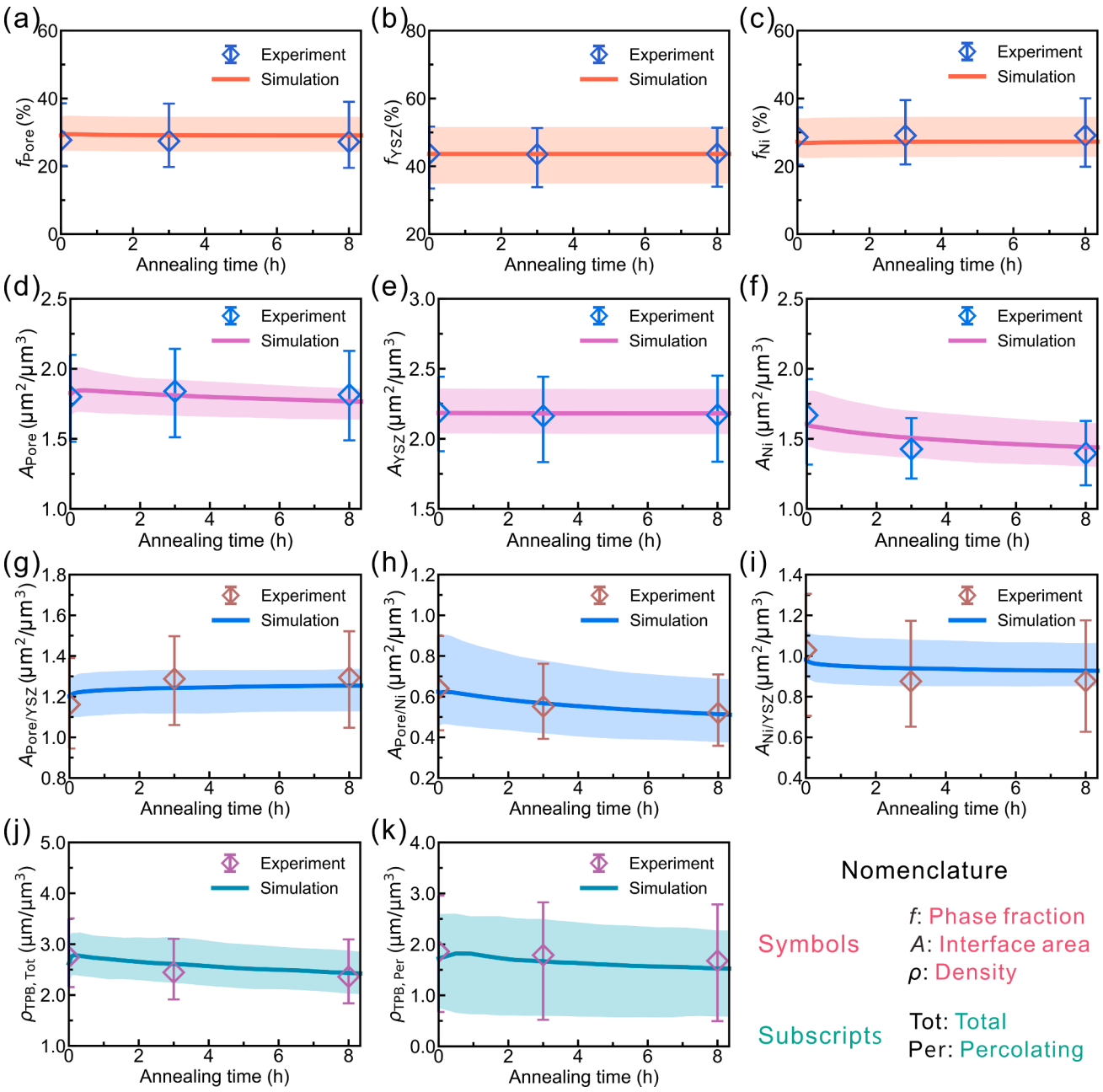

Fig. 3. Comparison of different microstructure parameters between the phase-field simulation results and the experimental data for the small sub-volumes with the domain of $3.7 \times 3.7 \times 3.7$ **μm**^{3}. Phase fractions of (a) pore, (b) YSZ and (c) Ni; Interface areas per unit volume of (d) pore, (e) YSZ and (f) Ni; Interface areas per unit volume of (g) pore/YSZ, (h) pore/Ni and (i) Ni/YSZ; (j) total TPB density and (k) percolating TPB density. The line with the uncertainty region denotes the phase-field simulated results, while the marker with the error bar denotes the experimental data.

different locations of the real Ni-YSZ electrode microstructure, and their values are within the estimated errors of both experiment and simulation. Therefore, the phase-field simulations of the large number small sub-volumes validated the reliability of the thermophysical parameters obtained by the simulation of the isolated Ni particle.

4.2. Ni coarsening in Ni-YSZ electrode

Two sub-volumes with a medium domain of $5.5 \times 5.5 \times 5.5$ μm^3 and a large domain of $9.2 \times 9.2 \times 5.5$ μm^3 taken from the experimental microstructure of the real Ni-YSZ electrode at 0 h (see Fig. 1c and d) were used as the initial input of phase-field simulation, and those at 3 h and 8 h for validation of subsequent simulations. Moreover, the medium sub-volume is inside the large sub-volume (see Fig. 1c). Based on the thermophysical parameters obtained previously (described in Section 2.1), the 3D quantitative phase-field simulations of Ni coarsening in these medium and large sub-volumes were performed.

4.2.1. Microstructure evolution

A variety of 2D microstructures were obtained by cutting the 3D microstructure along certain planes. The 2D microstructures from the 3D phase-field simulated medium and large sub-volumes at different annealing times were compared with those from the experimental microstructures of the Ni-YSZ electrode after the same annealing time. Fig. 4 displays the comparison of 2D microstructures obtained by cutting 3D phase-field simulated and experimental microstructures along a typical plane. As shown in Fig. 4, it is seen that small Ni particles gradually disappear (A, B, C and D regions) as the annealing time

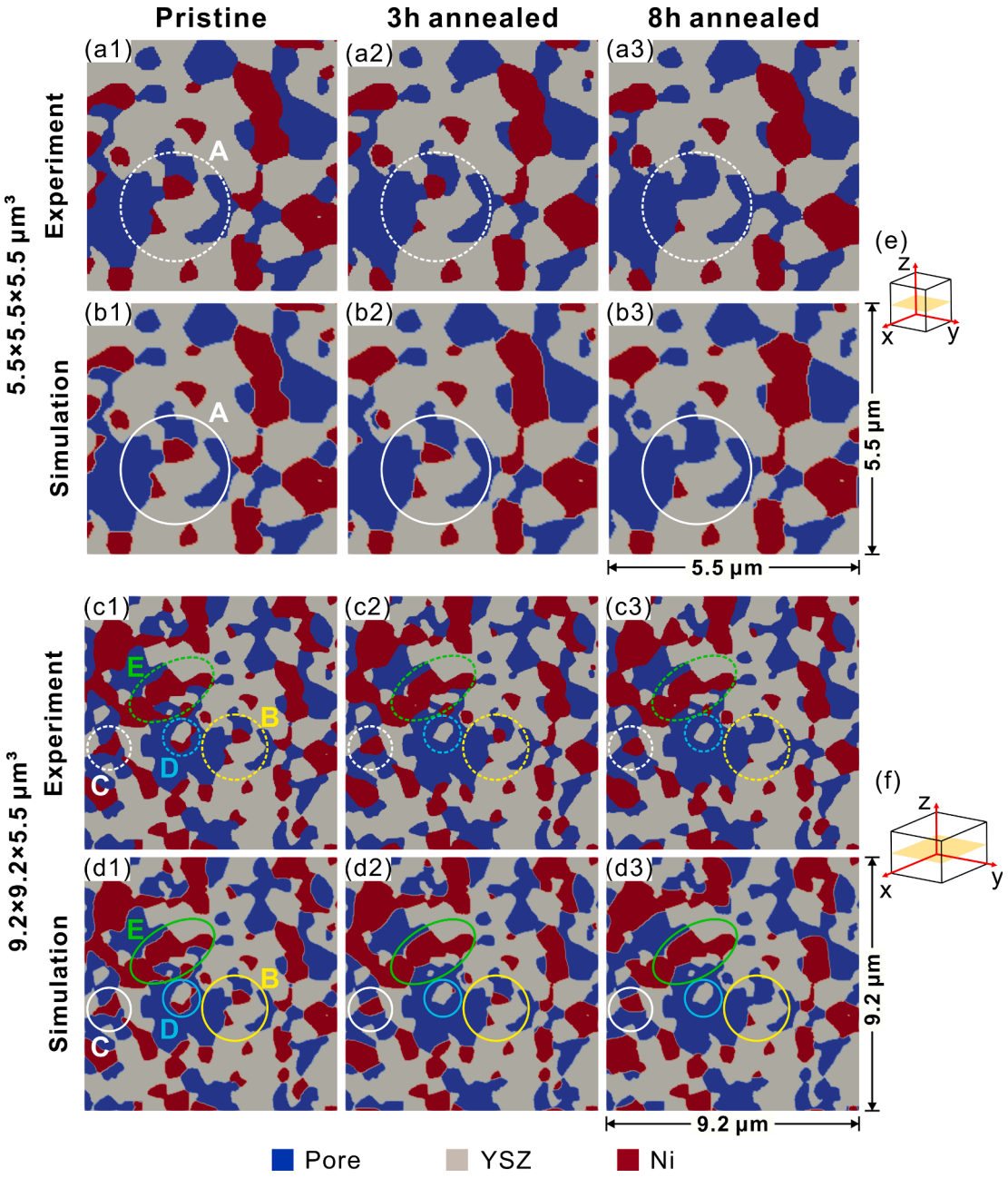

Fig. 4. 2D microstructures revealed by cutting 3D microstructure along certain planes. (a1–a3) and (b1–b3) 2D cuts from the experimental and phase-field simulated 3D microstructures with a medium domain of $5.5 \times 5.5 \times 5.5$ **μm**^{3}, respectively, while (c1–c3) and (d1–d3) 2D cuts from experimental and phase-field simulated 3D microstructures with a large domain of $9.2 \times 9.2 \times 5.5$ **μm**^{3}, respectively. The yellow planes in (e) medium and (f) large sub-volumes schematically denote the 2D cutting plane from corresponding 3D sub-volumes. (For interpretation of the references to colour in this figure legend, the reader is referred to the web version of this article.).

increases and the large Ni particle appears to coarsen (the E region surrounded by the green circle). The YSZ structure does not evolve detectably and provides a static backbone for the Ni and pore phases to move around it. Most of the microstructure changes happen within the first 3 h of annealing, only minor additional change is observed from 3 h to 8 h. Moreover, the local microstructures inside the central region of the simulated volumes are consistent with the experimental results, while those close to the boundary of simulated sub-volumes are different. The evolution of the local microstructure is extremely sensitive to its surrounding microstructure. At the boundary, discrete solutions of partial differential equations in the phase-field model need to be supplemented by the boundary conditions, and thus the surrounding microstructure in the simulation is different from the experimental one, resulting in the difference after 3 h and 8 h annealing. The deviation between the phase-field simulation and experiment results gets smaller in the case of the large sub-volume due to the smaller ratio between the microstructure at its boundaries and its internal microstructure.

A direct 3D comparison of phase-field simulated and experimental microstructures for the medium and large sub-volumes was performed. The parameter to distinguish the simulated and experimental microstructures ($\delta_{\text{dis}}(t, \vec{x})$) was calculated and shown in Fig. 5. From Fig. 5, it can be seen that the $\delta_{\text{dis}}(t, \vec{x})$ in the pristine state is always equal to 0, 4 or 8 (i.e., pore, YSZ or Ni respectively) since the simulated microstructures in the pristine state are identical to the experimental ones. For the pore phase in the simulated microstructure (i.e., $\phi_{\text{sim}}(t, \vec{x}) = 0$), the

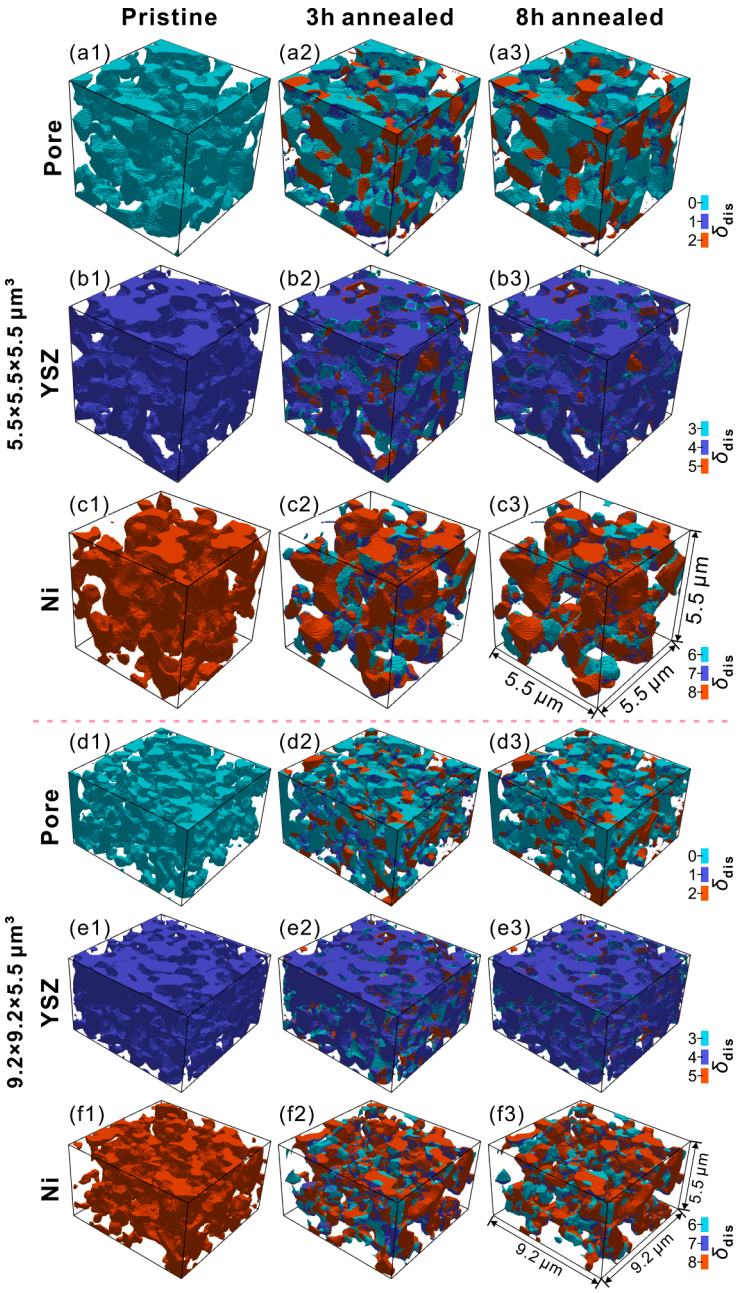

Fig. 5. Comparison of phase-field simulated and experimental 3D microstructures. $\boldsymbol{\delta_{dis}}(t, \vec{x})$ for (a1–a3 and d1–d3) pore, (b1–b3 and e1–e3) YSZ, and (c1–c3 and f1–f3) Ni phases in phase-field simulated 3D microstructures with a medium domain of (a1–a3, b1–b3 and c1–c3) $5.5 \times 5.5 \times 5.5$ $\boldsymbol{\mu m}^3$ and a large domain of (d1–d3, e1–e3 and f1–f3) $9.2 \times 9.2 \times 5.5$ $\boldsymbol{\mu m}^3$ in the pristine state (a1, b1, c1, d1, e1 and f1), after annealing for 3 h (a2, b2, c2, d2, e2 and f2) and for 8 h (a3, b3, c3, d3, e3 and f3).

$\delta_{dis}(t, \vec{x})$ is 0 for most of grid points and 1 and 2 for a few grid points after annealing for 3 h and for 8 h (see Fig. 5 (a2, a3, d2 and d3)), i.e., the $\phi_{exp}(t, \vec{x})$ is 0 for most of grid points and 1 and 2 for a few grid points. For the YSZ phase in the simulated microstructure (i.e., $\phi_{sim}(t, \vec{x}) = 1$), the $\delta_{dis}(t, \vec{x})$ is 4 for most of grid points and 3 and 5 for a few grid points after annealing for 3 h and for 8 h (see Fig. 5 (b2, b3, e2 and e3)), i.e., the $\phi_{exp}(t, \vec{x})$ is 1 for most of grid points and 0 and 2 for a few grid points. For the Ni phase in the simulated microstructure (i.e., $\phi_{sim}(t, \vec{x}) = 2$), the $\delta_{dis}(t, \vec{x})$ is 8 for most of grid points and 6 and 7 for a few grid points after annealing for 3 h and for 8 h (see Fig. 5 (c2, c3, f2 and f3)), i.e., the $\phi_{exp}(t, \vec{x})$ is 2 for most of grid points and 0 and 1 for a few grid points.

To quantify the comparison between the simulated and experimental microstructures, the δ_{dis} of their comparison (shown in Fig. 5) was statistically analyzed and the probability of δ_{dis} was plotted in Fig. 6. The probabilities of the $\delta_{dis}(t, \vec{x}) = 0$, 4 and 8 (i.e., pore, YSZ and Ni, respectively) in medium and large sub-volumes are 100% in the pristine state. For the pore phase in the simulated microstructure, the probabilities of $\delta_{dis}(t, \vec{x}) = 0$, 1 and 2 are about 82–84%, 4–6%, and 10–14% after annealing for 3 h and for 8 h, respectively. This indicates the evolution of the pore phase in the phase-field simulated microstructure agrees with that in the corresponding experimental microstructure. For the YSZ phase in the simulated microstructure, the probabilities of $\delta_{dis}(t, \vec{x}) = 3$, 4 and 5 are about 3–5%, 92–95%, and 2–3% after annealing for 3 h and for 8 h, respectively. This indicates the YSZ evolution in the phase-field simulated microstructure agrees well with that in the

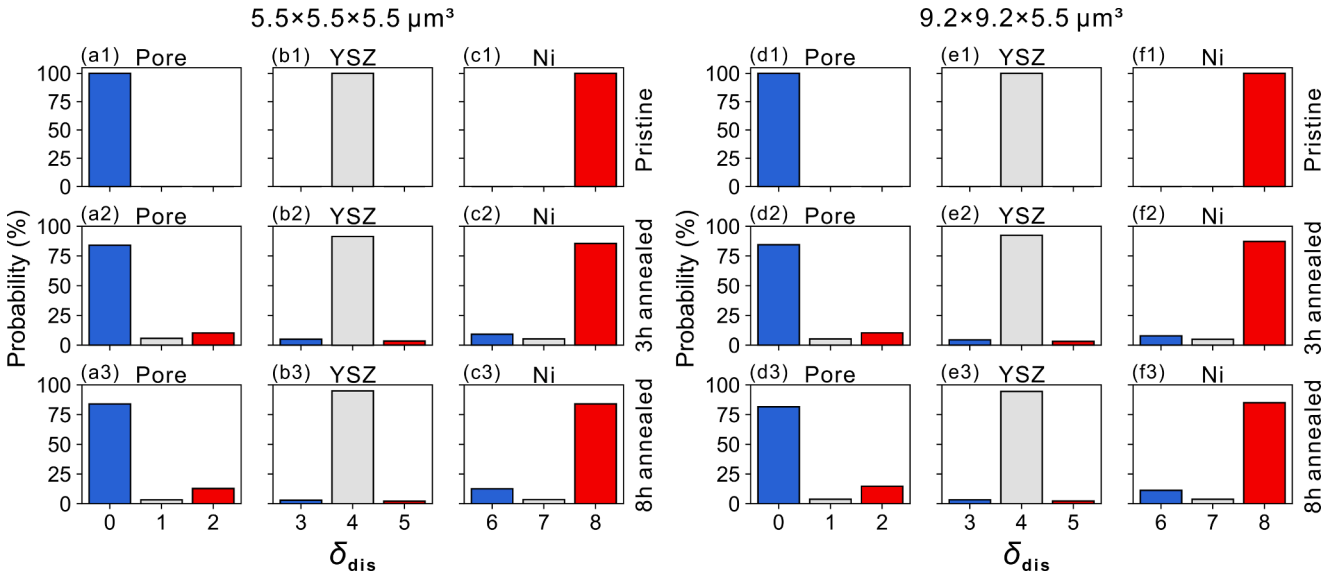

Fig. 6. Statistical probability of $\boldsymbol{\delta}_{\mathbf{dis}}(t, \vec{x})$ for comparison of phase-field simulated and experimental 3D microstructures. Probability of $\boldsymbol{\delta}_{\mathbf{dis}}(t, \vec{x})$ for (a1–a3 and d1–d3) pore, (b1–b3 and e1–e3) YSZ, and (c1–c3 and f1–f3) Ni phases in phase-field simulated 3D microstructures with a medium domain of (a1–a3, b1–b3 and c1–c3) $5.5 \times 5.5 \times 5.5$ $\boldsymbol{\mu m}^3$ and a large domain of (d1–d3, e1–e3 and f1–f3) $9.2 \times 9.2 \times 5.5$ $\boldsymbol{\mu m}^3$ in the pristine state (a1, b1, c1, d1, e1 and f1), after annealing for 3 h (a2, b2, c2, d2, e2 and f2) and for 8 h (a3, b3, c3, d3, e3 and f3).

corresponding experimental microstructure. For the Ni phase in the simulated microstructure, the probabilities of $\delta_{\mathrm{dis}}(t, \vec{x}) = 6$, 7 and 8 are about 8–13%, 3–5%, and 84–87% after annealing for 3 h and for 8 h, respectively. This indicates the Ni evolution in the phase-field simulated microstructure agrees with that in the corresponding experimental microstructure. In summary, there is on average an approximate error in the order of 10% in the discrepancy between the simulated and experimental data and there is no systematic trend in the error for all phases as a function of annealing time. A good point to highlight is that the model closely follows the experimental results in the 0–8 h annealing time frame, which gives confidence in using the model to make predictions at longer time by coupling with some key experimental validation.

The deviations between the phase-field simulations and the experimental data can be due to errors both in the simulation and the reconstructed experimental microstructures. Experimentally, the sample was cooled down before imaging during each heating cycle, which may lead to the imaged microstructure not being exactly representative of an isothermal heat treatment that the phase-field simulation represents. Furthermore, there is the systematic error in the experimental reconstruction will always be present due to the image analysis operations to produce the three-phase segmentation of greyscale electron density based ptychographic 3D image volumes. For the simulation, the error due to the boundary effect of discrete solutions of partial differential equations in the phase-field model always exists. The usage of a larger order of the spatial resolution in the simulation to improve computational efficiency will increase the error of the grid points at the boundaries. Moreover, the numerical diffusion interface in phase-field simulated microstructures was directly compared with the experimental microstructures (approximated as the sharp phase interface), which may lead to the discrepancy between simulation and experimental microstructures. If these errors were eliminated, the probabilities of $\delta_{\mathrm{dis}}(t, \vec{x}) = 0$, 4 and 8 can get larger, while probabilities of $\delta_{\mathrm{dis}}(t, \vec{x}) = 1$, 2, 3, 5, 6 and 7 can get smaller, i.e., the phase-field simulation results can be more consistent with the experimental ones.

4.2.2. Statistical analysis of microstructure

The microstructure parameters of phase-field simulated medium and large sub-volumes during annealing were calculated and their comparison with the experimental results is displayed in Fig. 7. The effect of microstructural heterogeneity on microstructure parameters of the large sub-volume was not considered, but its effect on the medium sub-volume was still considered. Thus, in order to validate phase-field simulated results of the medium sub-volume, the microstructure parameters of more than 120 medium sub-volumes taken from different locations within the real experimental microstructure were calculated, and their maximum and minimum values were used as the upper and lower limits of the uncertainty. From Fig. 7, it can be seen that phase fractions of pore, YSZ and Ni, interface areas of pore, YSZ and Ni per unit volume, interface areas of pore/YSZ, pore/Ni and Ni/YSZ per unit volume, total TPB density and percolating TPB density in the medium and large sub-volumes show the same trend with the annealing time as in the case of the small sub-volume (Fig. 3). Besides the microstructure parameters, the connected phase fractions of pore, YSZ and Ni phases were calculated. From Fig. 7j–l, it is observed that the connected phase fractions of the pore phase in medium and large sub-volumes increase as the annealing time increases, those of the YSZ phase do not change, while those of the Ni phase decrease. Overall, the microstructure parameters from the simulation are compatible with the experimental data, also for the medium and large sub-volumes.

The PSDs for Ni, pore and YSZ phases in the medium and large sub-volumes were calculated, and direct comparisons between those of phase-field simulation and experimental sub-volumes were performed. Fig. 8 presents the PSDs for Ni, pore and YSZ phases for the medium and large sub-volumes in the pristine state and after 3 h and 8 h of annealing. The PSD curves of the pore phase in medium and large sub-volumes evolve slightly with time, those of the YSZ phase look almost identical, and those of the Ni phase move towards large particle size, indicating Ni particle coarsening. As also displayed in Fig. 8, the maximum absolute errors between the simulated and experimental results for PSDs of the pore phase at 3 h is about 9.4% and 9.3% in medium and large sub-volumes, respectively, while it becomes about 10.8% and 15.0% at 8 h. The absolute errors between simulated and experimental results for PSDs of the YSZ phase in medium and large sub-volumes during annealing are less than 1.9%. The maximum absolute errors between simulated and experimental results for PSDs of the Ni phase in medium and large sub-volumes at 3 h are about 17.4% and 16.1%, while those for PSDs of the Ni phase in those two sub-volumes at 8 h are about 11.9% and 8.6%. The coefficients of determination (R^2) between simulated and

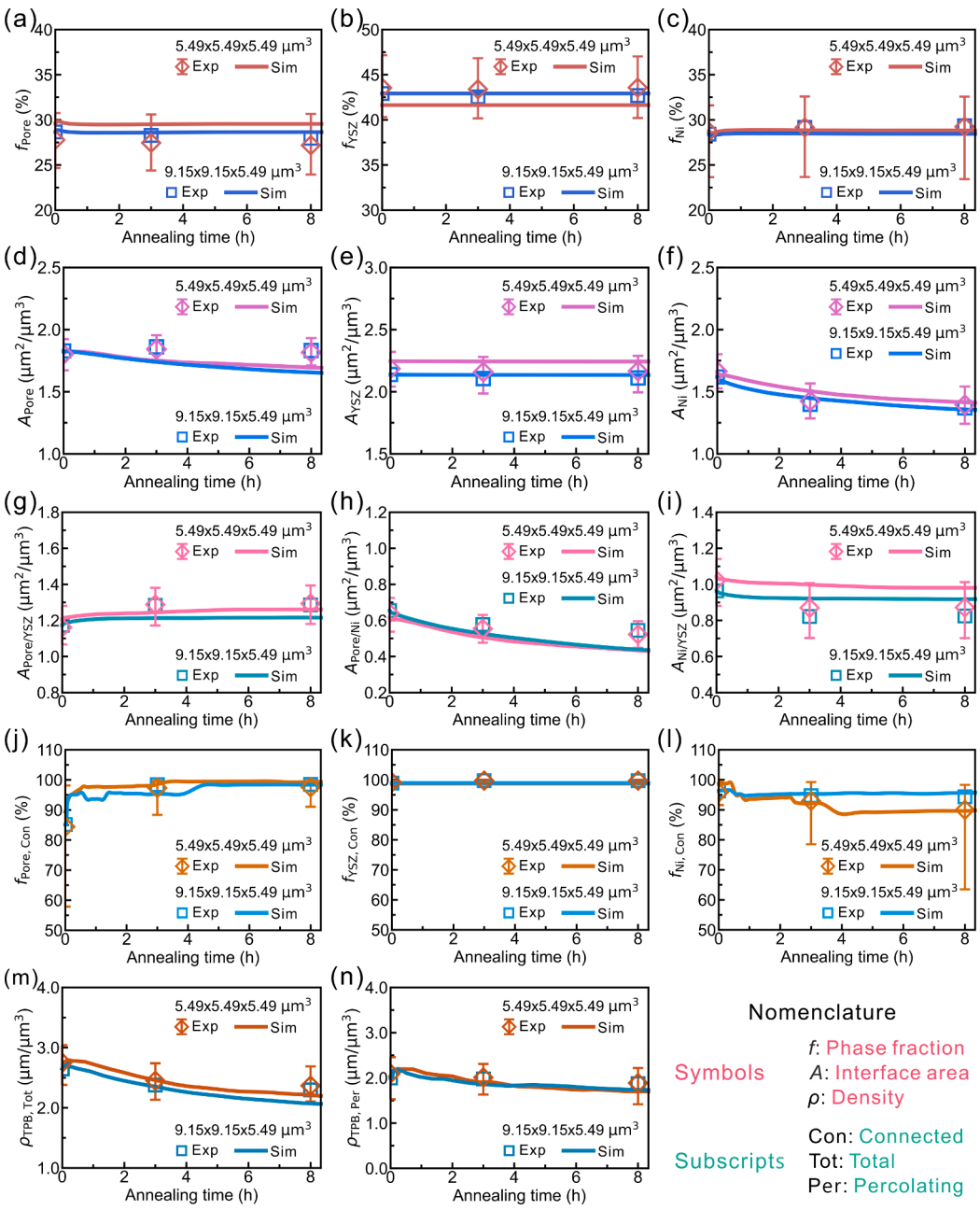

Fig. 7. Comparison of different microstructure parameters between the phase-field simulation results and the experimental data in a medium domain of $5.5 \times 5.5 \times 5.5$ **μm**^{3} and a large domain of $9.2 \times 9.2 \times 5.5$ **μm**^{3}. Phase fractions of (a) pore, (b) YSZ and (c) Ni; Interface areas per unit volume of (d) pore, (e) YSZ and (f) Ni; Interface areas per unit volume of (g) pore/YSZ, (h) pore/Ni and (i) Ni/YSZ; Phase fractions of connected (j) pore, (k) YSZ and (l) Ni; (m) total TPB density and (n) percolating TPB density.

experimental PSDs for all phases in medium and large sub-volumes at different annealing times were calculated. The R^2 between simulated and experimental PSDs of the pore, YSZ and Ni phases at 0 h are 1.0 in medium and large sub-volumes, and those of the YSZ phase at annealing states are also almost equal to 1.0 ($\geq$0.9998) in both sub-volumes. The R^2 between simulated and experimental PSDs of the pore phase in medium and large sub-volumes at 3 h and 8 h are larger than 0.980, while those of the Ni phase in medium and large sub-volumes at 3 h and 8 h are larger than 0.970. The R^2 between simulated and experimental PSDs of the Ni phase in the large sub-volume is larger than that of the Ni phase in the medium sub-volume. This indicates that the simulation agrees better with the experimental data in the large sub-volume than in the medium sub-volume on the evolution of Ni coarsening.

The evolution of TPB tortuosity for Ni, pore and YSZ phases in the medium and large sub-volumes was analyzed, and direct comparisons between those of phase-field simulation and experimental sub-volumes were performed. As shown in Fig. 9, the TPB sites for the pore phase in medium and large sub-volumes increase when the TPB tortuosity is less than 1.3 as the annealing time increases, those for the YSZ phase do not change significantly, and those for the Ni phase decrease when TPB tortuosity is less than 1.3. As displayed in Fig. 9, the maximum absolute errors between simulated and experimental results for TPB sites of the pore phase in medium and large sub-volumes during annealing are about 2%, while those for TPB sites of the YSZ and Ni phases in those two sub-volumes during annealing are about 1%. The absolute errors of phase-field simulated and experimental results for TPB sites of pore and Ni phases are less than 1% when the TPB tortuosity is larger than 1.3. The R^2 between simulated and experimental TPB sites for all phases in medium and large sub-volumes at different annealing times were calculated. The R^2 between simulated and experimental TPB sites of the pore, YSZ and Ni phases at 0 h are 1.0 in medium and large sub-volumes, and those of the YSZ phase at annealing states are larger than 0.997 in both sub-volumes. The R^2 between simulated and experimental TPB sites of the pore phase in medium and large sub-volumes at 3 h and 8 h

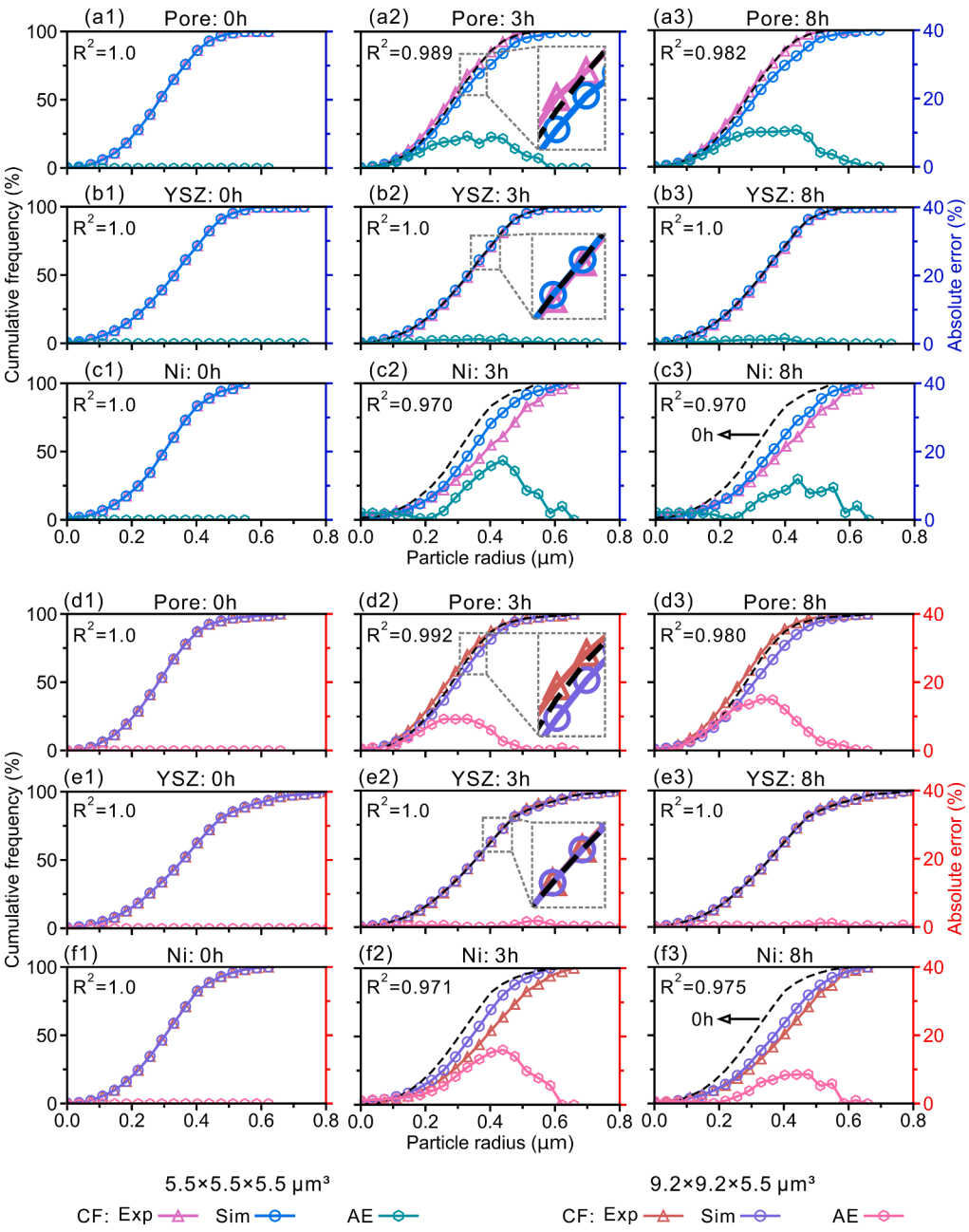

Fig. 8. Comparison of phase-field simulated and experimental cumulative PSDs of pore, YSZ and Ni phases. Cumulative PSDs of (a1–a3) pore, (b1–b3) YSZ and (c1–c3) Ni phases in the microstructures with a medium domain of $5.5 \times 5.5 \times 5.5\ \mu m^3$. Cumulative PSDs of (d1–d3) pore, (e1–e3) YSZ and (f1–f3) Ni phases in the microstructures with a large domain of $9.2 \times 9.2 \times 5.5\ \mu m^3$. The left *y*-axis is the cumulative frequency (CF), while the right *y*-axis is the absolute error (AE) between the phase-field simulated results and the experimental data. "Exp" denotes the experimental results, while "Sim" denotes the simulation ones. The black dashed line indicates the cumulative PSD of three phases at 0 h for comparison with those at 3 h and 8 h in the subplot.

are larger than 0.949, while those of the Ni phase in medium and large sub-volumes at 3 h and 8 h are larger than 0.988. The R^2 between simulated and experimental TPB sites of the Ni phase in the large sub-volume is larger than that of the Ni phase in the medium sub-volume. This indicates that the simulation agrees better with the experimental data in the large sub-volume than in the medium sub-volume on the evolution of TPB tortuosity for the Ni phase.

5. Conclusions

- A strategy of 3D phase-field simulation using the MPF model coupled with reliable thermophysical parameters and *ex-situ* experiment was proposed for the quantitative description of Ni coarsening in Ni-YSZ electrodes. With this strategy, the quantitative phase-field simulation of Ni coarsening in Ni-YSZ electrodes was realized.
- Based on the phase-field simulation of a small 3D sub-volume (i.e., the domain of $3.7 \times 3.7 \times 3.7\ \mu m^3$) with an isolated Ni particle calibrated with the experimental data, a set of material parameters were obtained. Their reliability was further confirmed through a comprehensive comparison between the phase-field simulation of twelve 3D small sub-volumes taken from different locations in the experimental microstructure of the Ni-YSZ electrode and the corresponding experimental data.
- Two 3D sub-volumes, i.e., the medium domain of $5.5 \times 5.5 \times 5.5\ \mu m^3$ and large domain of $9.2 \times 9.2 \times 5.5\ \mu m^3$, taken from the initial pristine experimental microstructure were used for phase-field simulation. A direct comparison of the simulated 3D microstructures with the subsequent experimental ones at annealing time steps was implemented, and their consistency was quantified. Moreover, the various characteristic information of 3D microstructures including microstructure parameters, PSDs and TPB tortuosity, were statistically analyzed and comprehensively compared. A good agreement between phase-field simulation and experimental results was

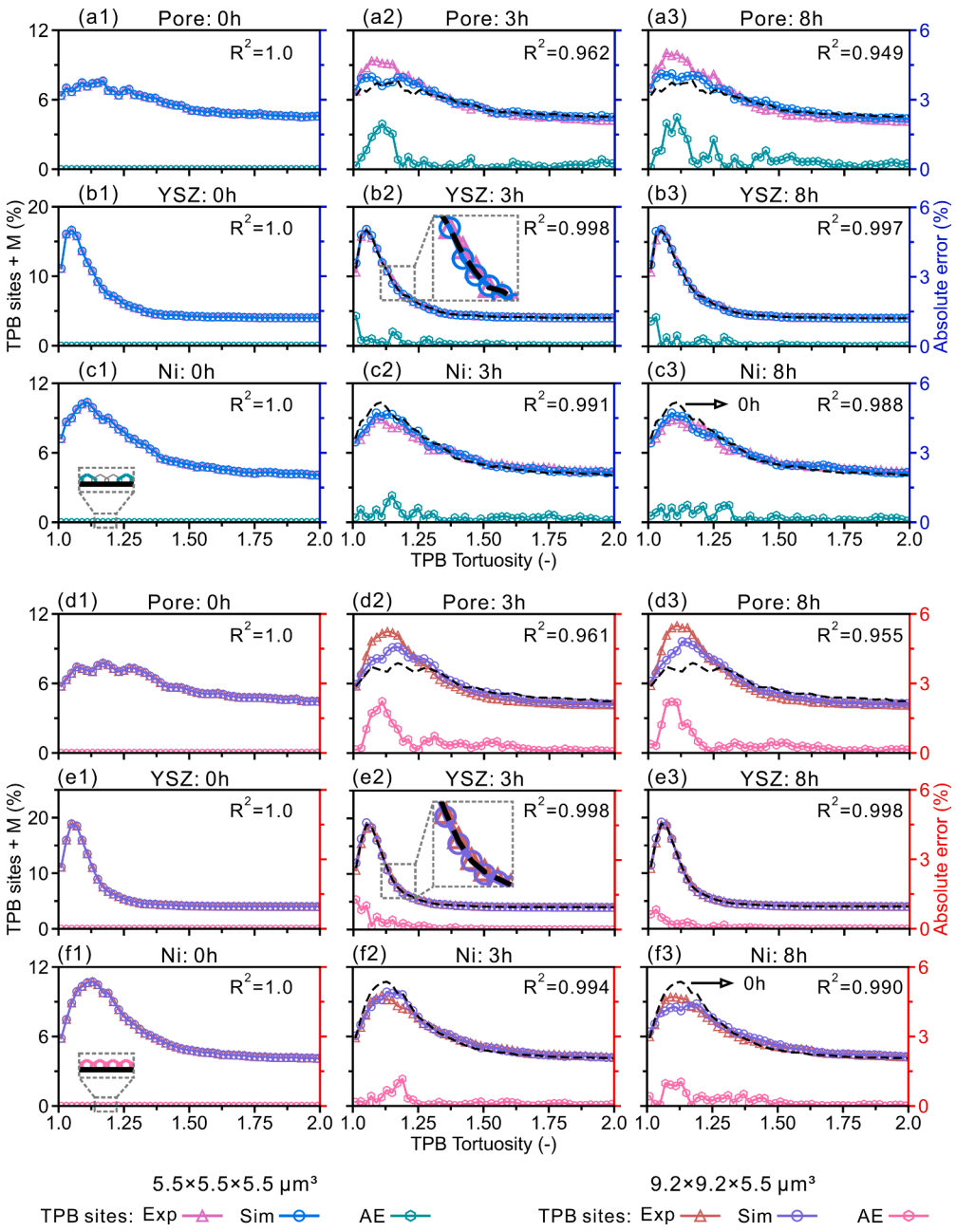

Fig. 9. Comparison of phase-field simulated and experimental TPB tortuosity evolution of pore, YSZ and Ni phases. TPB tortuosity evolution of (a1–a3) pore, (b1–b3) YSZ and (c1–c3) Ni phases in the microstructures with a medium domain of $5.5 \times 5.5 \times 5.5$ **μm**^{3}. TPB tortuosity evolution of (d1–d3) pore, (e1–e3) YSZ and (f1–f3) Ni phases in the microstructures with a large domain of $9.2 \times 9.2 \times 5.5$ **μm**^{3}. The left *y*-axis is the TPB sites, while the right *y*-axis is the absolute error (AE) between the phase-field simulated results and the experimental data. "Exp" denotes the experimental results, while "Sim" denotes the simulation ones. "M" (in "TPB sites + M") indicates the value at which the TPB site was moved to avoid the overlapping of curves, given as 4%. The black dashed line indicates the cumulative PSD of three phases at 0 h for comparison with those at 3 h and 8 h in the subplot.

achieved, and the phase-field simulation results performed in the large sub-volume were more consistent with experimental ones.

- The reliable time evolution of the TPB density of Ni-YSZ electrodes obtained by phase-field simulations can be used as input of an electrochemical model, and thus the time evolution of the electrochemical property of the Ni-YSZ electrode can be predicted. Combining phase-field-electrochemical simulations with artificial structure generators can be used in the future to model the performance of hypothetical structures to predict optimum electrode designs.
- The presently proposed strategy for the quantitative phase-field simulation is anticipated to be applicable in Ni coarsening of other types of Ni-YSZ based electrodes for SOCs, like Ni/Scandia-and-Yttria-doped-Zirconia (Ni-ScYSZ), and also other degradation behaviors of Ni-YSZ based electrodes during operation, e.g., Ni migration.

Declaration of Competing Interest

The authors declare that they have no known competing financial interests or personal relationships that could have appeared to influence the work reported in this paper.

Acknowledgments

This work was supported by the project "Efficient Power2Gas Combining SOEC and Biomass Gasification" (EUDP no. 64017–0011). Shenglan Yang acknowledges the China Scholarship Council (CSC No: 201906370120). Lijun Zhang acknowledges the financial support from the Natural Science Foundation of Hunan Province for Distinguished Young Scholars (Grant No. 2021JJ10062).

Supplementary materials

Supplementary material associated with this article can be found, in the online version, at doi:10.1016/j.actamat.2023.118708.

References

[1] C. Graves, S.D. Ebbesen, S.H. Jensen, S.B. Simonsen, M.B. Mogensen, Eliminating degradation in solid oxide electrochemical cells by reversible operation, Nat. Mater. 14 (2) (2015) 239–244.

[2] M.S. Khan, S.B. Lee, R.H. Song, J.W. Lee, T.H. Lim, S.J. Park, Fundamental mechanisms involved in the degradation of nickel–yttria stabilized zirconia (Ni–YSZ) anode during solid oxide fuel cells operation: a review, Ceram. Int. 42 (1) (2016) 35–48.

[3] T.L. Skafte, J. Hjelm, P. Blennow, C. Graves, Quantitative review of degradation and lifetime of solid oxide cells and stacks, in: Proceedings of the 12th European SOFC & SOE Forum, 2016, pp. 8–27.

[4] S. Koch, P.V. Hendriksen, M. Mogensen, Y.L. Liu, N. Dekker, B. Rietveld, B. De Haart, F. Tietz, Solid oxide fuel cell performance under severe operating conditions, Fuel Cells 6 (2) (2006) 130–136.

[5] D. Simwonis, F. Tietz, D. Stöver, Nickel coarsening in annealed Ni/8YSZ anode substrates for solid oxide fuel cells, Solid State Ionics 132 (3-4) (2000) 241–251.

[6] L. Holzer, B. Iwanschitz, T. Hocker, B. Münch, M. Prestat, D. Wiedenmann, U. Vogt, P. Holtappels, J. Sfeir, A. Mai, Microstructure degradation of cermet anodes for solid oxide fuel cells: quantification of nickel grain growth in dry and in humid atmospheres, J. Power Sources 196 (3) (2011) 1279–1294.

[7] A. Faes, A. Hessler-Wyser, D. Presvytes, C. Vayenas, J. Van Herle, Nickel–zirconia anode degradation and triple phase boundary quantification from microstructural analysis, Fuel Cells 9 (6) (2009) 841–851.

[8] P. Tanasini, M. Cannarozzo, P. Costamagna, A. Faes, J. Van Herle, A. Hessler-Wyser, C. Comninellis, Experimental and theoretical investigation of degradation mechanisms by particle coarsening in SOFC electrodes, Fuel Cells 9 (5) (2009) 740–752.

[9] M.Z. Khan, M.T. Mehran, R.H. Song, J.W. Lee, S.B. Lee, T.H. Lim, A simplified approach to predict performance degradation of a solid oxide fuel cell anode, J. Power Sources 391 (2018) 94–105.

[10] J.S. Cronin, J.R. Wilson, S.A. Barnett, Impact of pore microstructure evolution on polarization resistance of Ni-Yttria-stabilized zirconia fuel cell anodes, J. Power Sources 196 (5) (2011) 2640–2643.

[11] Z. Jiao, N. Shikazono, N. Kasagi, Quantitative characterization of SOFC nickel-YSZ anode microstructure degradation based on focused-ion-beam 3D-reconstruction technique, J. Electrochem. Soc. 159 (3) (2012) B285.

[12] Y.H. Lee, H. Muroyama, T. Matsui, K. Eguchi, Degradation of nickel–yttria-stabilized zirconia anode in solid oxide fuel cells under changing temperature and humidity conditions, J. Power Sources 262 (2014) 451–456.

[13] G. Brus, H. Iwai, A. Sciazko, M. Saito, H. Yoshida, J.S. Szmyd, Local evolution of anode microstructure morphology in a solid oxide fuel cell after long-term stack operation, J. Power Sources 288 (2015) 199–205.

[14] M. Trini, P. Jørgensen, A. Hauch, J. Bentzen, P. Hendriksen, M. Chen, 3D microstructural characterization of Ni/YSZ electrodes exposed to 1 year of electrolysis testing, J. Electrochem. Soc. 166 (2) (2019) F158.

[15] G.J. Nelson, K.N. Grew, J.R. Izzo Jr, J.J. Lombardo, W.M. Harris, A. Faes, A. Hessler-Wyser, S. Wang, Y.S. Chu, A.V. Virkar, Three-dimensional microstructural changes in the Ni–YSZ solid oxide fuel cell anode during operation, Acta Mater. 60 (8) (2012) 3491–3500.

[16] E. Lay-Grindler, J. Laurencin, J. Villanova, P. Cloetens, P. Bleuet, A. Mansuy, J. Mougin, G. Delette, Degradation study by 3D reconstruction of a nickel–yttria stabilized zirconia cathode after high temperature steam electrolysis operation, J. Power Sources 269 (2014) 927–936.

[17] D. Kennouche, Y.C.K. Chen-Wiegart, C. Riscoe, J. Wang, S.A. Barnett, Combined electrochemical and X-ray tomography study of the high temperature evolution of Nickel–Yttria Stabilized Zirconia solid oxide fuel cell anodes, J. Power Sources 307 (2016) 604–612.

[18] S. De Angelis, P.S. Jørgensen, E.H.R. Tsai, M. Holler, K. Kreka, J.R. Bowen, Three dimensional characterization of nickel coarsening in solid oxide cells via *ex-situ* ptychographic nano-tomography, J. Power Sources 383 (2018) 72–79.

[19] L.Q. Chen, Phase-field models for microstructure evolution, Annu. Rev. Mater. Res. 32 (1) (2002) 113–140.

[20] I. Steinbach, Phase-field models in materials science, Modell. Simul. Mater. Sci. Eng. 17 (7) (2009), 073001.

[21] N. Provatas, K. Elder, Phase-Field Methods in Materials Science and Engineering, John Wiley & Sons, 2011.

[22] Y. Li, S. Hu, X. Sun, M. Stan, A review: applications of the phase field method in predicting microstructure and property evolution of irradiated nuclear materials, npj Comput. Mater. 3 (1) (2017) 1–17.

[23] E. Miyoshi, T. Takaki, M. Ohno, Y. Shibuta, S. Sakane, T. Shimokawabe, T. Aoki, Ultra-large-scale phase-field simulation study of ideal grain growth, npj Comput. Mater. 3 (1) (2017) 1–6.

[24] S. Yang, J. Zhong, M. Chen, L. Zhang, A parametric three-dimensional phase-field study of the physical vapor deposition process of metal thin films aiming at quantitative simulations, Coatings 9 (10) (2019) 607.

[25] J. Gao, A. Malchère, S. Yang, A. Campos, T. Luo, K. Quertite, P. Steyer, C. Girardeaux, L. Zhang, D. Mangelinck, Dewetting of Ni silicide thin film on Si substrate: *in-situ* experimental study and phase-field modeling, Acta Mater. 223 (2022), 117491.

[26] S. Yang, J. Zhong, J. Wang, J. Gao, Q. Li, L. Zhang, A novel computational model for isotropic interfacial energies in multicomponent alloys and its coupling with phase-field model with finite interface dissipation, J. Mater. Sci. Technol. 133 (2023) 111–122.

[27] H.Y. Chen, H.C. Yu, J.S. Cronin, J.R. Wilson, S.A. Barnett, K. Thornton, Simulation of coarsening in three-phase solid oxide fuel cell anodes, J. Power Sources 196 (3) (2011) 1333–1337.

[28] T. Abdullah, L. Liu, Phase field simulation coupling microstructural evolution and crack propagation during performance degradation of solid oxide fuel cells, ECS Trans. 66 (2) (2015) 207.

[29] R. Davis, F. Abdeljawad, J. Lillibridge, M. Haataja, Phase wettability and microstructural evolution in solid oxide fuel cell anode materials, Acta Mater. 78 (2014) 271–281.

[30] Z. Jiao, N. Shikazono, Prediction of nickel morphological evolution in composite solid oxide fuel cell anode using modified phase field model, J. Electrochem. Soc. 165 (2) (2018) F55.

[31] M. Trini, S. De Angelis, P.S. Jørgensen, P.V. Hendriksen, K. Thornton, M. Chen, Towards the validation of a phase field model for Ni coarsening in solid oxide cells, Acta Mater. 212 (2021), 116887.

[32] Y. Lei, T.L. Cheng, H. Abernathy, W. Epting, T. Kalapos, G. Hackett, Y. Wen, Phase field simulation of anode microstructure evolution of solid oxide fuel cell through Ni $(OH)_2$ diffusion, J. Power Sources 482 (2021), 228971.

[33] A. Bueno-Orovio, V.M. Pérez-García, Spectral smoothed boundary methods: the role of external boundary conditions, Numer. Methods Partial Differ. Equ. 22 (2) (2006) 435–448.

[34] L. Gránásy, T. Pusztai, D. Saylor, J.A. Warren, Phase field theory of heterogeneous crystal nucleation, Phys. Rev. Lett. 98 (3) (2007), 035703.

[35] L. Zhang, Y. Du, Phase-field model of finite interface dissipation: A novel way to directly couple with calphad databases, J. Phase Equilib. Diffus. 37 (2016) 259–260.

[36] J. Eiken, B. Böttger, I. Steinbach, Multiphase-field approach for multicomponent alloys with extrapolation scheme for numerical application, Phys. Rev. E 73 (6) (2006), 066122.

[37] I. Steinbach, F. Pezzolla, B. Nestler, M. Seeßelberg, R. Prieler, G.J. Schmitz, J. L. Rezende, A phase field concept for multiphase systems, Phys. D 94 (3) (1996) 135–147.

[38] N. Ta, L. Zhang, Y. Tang, W. Chen, Y. Du, Effect of temperature gradient on microstructure evolution in Ni–Al–Cr bond coat/substrate systems: a phase-field study, Surf. Coat. Technol. 261 (2015) 364–374.

[39] M. Wei, Y. Tang, L. Zhang, W. Sun, Y. Du, Phase-Field simulation of microstructure evolution in industrial A2214 alloy during solidification, Metall. Mater. Trans. A 46 (7) (2015) 3182–3191.

[40] S.L. Ebbehøj, T. Ramos, M. Mogensen, Impact of reduction parameters on the initial performance and stability of Ni/(Sc) YSZ cermet anodes for SOFCs, ECS Trans. 45 (1) (2012) 363.

[41] M. Holler, J. Raabe, A. Diaz, M. Guizar-Sicairos, C. Quitmann, A. Menzel, O. Bunk, An instrument for 3D x-ray nano-imaging, Rev. Sci. Instrum. 83 (7) (2012), 073703.

[42] J. Blakely, H. Mykura, Surface self diffusion measurements on nickel by the mass transfer method, Acta Metall. 9 (1) (1961) 23–31.

[43] P.S. Jørgensen, S.L. Ebbehøj, A. Hauch, Triple phase boundary specific pathway analysis for quantitative characterization of solid oxide cell electrode microstructure, J. Power Sources 279 (2015) 686–693.

[44] A. Tsoga, P. Nikolopoulos, Surface and grain-boundary energies in yttria-stabilized zirconia (YSZ-8 mol%), J. Mater. Sci. 31 (20) (1996) 5409–5413.

[45] H. Meltzman, D. Chatain, D. Avizemer, T.M. Besmann, W.D. Kaplan, The equilibrium crystal shape of nickel, Acta Mater. 59 (9) (2011) 3473–3483.

[46] H. Nahor, H. Meltzman, W.D. Kaplan, Ni-YSZ (111) solid–solid interfacial energy, J. Mater. Sci. 49 (11) (2014) 3943–3950.

[47] P. Haremski, L. Epple, M. Wieler, P. Lupetin, R. Thelen, M.J. Hoffmann, A thermal grooving study of relative grain boundary energies of nickel in polycrystalline Ni and in a Ni/YSZ anode measured by atomic force microscopy, Acta Mater. 214 (2021), 116936.